Contribution of gravity waves to universal vertical wavenumber ($\sim m^{-3}$) spectra revealed by a gravity-wave-permitting general circulation model

Haruka Okui[1], Kaoru Sato[1], and Shingo Watanabe[2]

[1]Department of Earth and Planetary Science, Graduate School of Science, The University of Tokyo, Tokyo, Japan

[2]Japan Agency for Marine–Earth Science and Technology, Yokohama, Japan

Corresponding author: Haruka Okui (okui@eps.s.u-tokyo.ac.jp)

Key Points:

- Using a gravity-wave-permitting general circulation model, vertical wavenumber (m) spectra in the whole middle atmosphere were examined.
- Characteristics of the model-simulated m spectra of gravity waves are broadly consistent with observations.
- Disturbances other than gravity waves contribute substantially to the lowest m part of the $\sim m^{-3}$ range.

Index Terms

3255 Spectral analysis, 3332 Mesospheric dynamics, 3334 Middle atmosphere dynamics, 3363 Stratospheric dynamics, 3384 Acoustic-gravity waves

Key Words

Gravity waves, middle atmosphere, spectral analysis

Abstract

Observations with high vertical resolution have revealed that power spectra of horizontal wind and temperature fluctuations versus vertical wavenumber m have a universal shape with a steep slope in a high m range, approximately proportional to m^{-3}. Several theoretical models explaining this spectral slope were proposed under an assumption of gravity wave (GW) saturation. However, little evidence has been obtained to show that these universal spectra are fully composed of GWs. To confirm the validity of this assumption, two kinds of m spectra are calculated using outputs from a GW-permitting high-top general circulation model. One is the spectra for GWs designated by fluctuations having total horizontal wavenumbers of 21–639. The other is the spectra of fluctuations unfiltered except extracting a linear trend in the vertical that were often analyzed in the observational studies. Comparison between the two shows that GWs dominate the observed spectra only in a higher m part of the steep slope, whereas disturbances other than GWs significantly contribute to its lower m part. Moreover, geographical distributions of the characteristic wavenumbers, slopes, and spectral densities of GW spectra are examined for several divided height regions of the whole middle atmosphere. It is shown that strong vertical shear below the zonal wind jets as well as the wave saturation is responsible for the formation of the steep slopes of GW spectra.

Plain Language Summary

Radar, lidar, and radiosonde observations have revealed that vertical wavenumber power spectra of horizontal wind and temperature fluctuations have common shape with a steep slope. Several theoretical studies have explained this universality by assuming that these spectra are composed of saturated gravity waves. To confirm the validity of this assumption, spectral analysis of gravity waves, having short horizontal wavelengths, was conducted using a gravity-wave-permitting high-top general circulation model. Comparison of the spectra of gravity waves with those of all model-simulated disturbances showed that disturbances other than gravity waves significantly contribute to the spectra in a low vertical-wavenumber part of the steep slope. Moreover, vertical and geographical variations of characteristics of gravity wave spectra were described. It is inferred that strong vertical shear below the eastward and westward jets as well as the wave saturation is responsible for the formation of the steep slopes of gravity wave spectra. As well as deepening our understanding of gravity waves in the middle atmosphere, these findings may provide useful guidelines for improving parameterizations of gravity waves in climate models.

1 Introduction

Gravity waves (GWs) are small-scale atmospheric waves that play fundamental roles in determining the large-scale dynamic and thermal structure of the middle atmosphere by transporting momentum and energy (e.g., Fritts & Alexander, 2003). For example, GW forcing contributes substantially to both maintaining the weak wind layer near the mesopause and driving the meridional circulation in the mesosphere (e.g., Holton, 1983). Equatorial stratospheric and mesospheric quasi biennial oscillations (QBOs) are mainly driven by GWs originating from the troposphere (e.g., Sato & Dunkerton, 1997; Kawatani et al., 2010a, 2010b; Mayr et al., 1997; Ern et al., 2014). It has also been shown that GWs cause extension of the deep branches of the Brewer–Dobson circulation to higher latitudes, and determination of the location of the turnaround latitude of the circulation (e.g., Okamoto et al., 2011; Sato & Hirano, 2019).

On the basis of radar (e.g., VanZandt, 1985; Fritts & Chou, 1987; Tsuda et al., 1989, 1990), radiosonde (e.g., VanZandt, 1982; Allen & Vincent, 1995; Sato et al., 2003) and rocket (e.g., Dewan et al., 1984; Dewan & Good, 1986) observations, it has been shown that power spectra versus the vertical wavenumber (m) of horizontal wind and temperature fluctuations have common shape with a steep slope. These 'universal' spectra are roughly proportional to m^{-3}, with slight dependence on the latitude, in a m range higher than the characteristic wavenumber m_*. The universal spectra have also been reported by satellite observations. Some satellite observations have considerably high vertical resolutions, such as GPS radio occultation data (e.g., Tsuda et al., 2011; Noersomadi & Tsuda, 2016) and Constellation Observing System for Meteorology, Ionosphere and Climate (COSMIC) (e.g., Yan et al. 2018). However, their horizontal resolutions are in general not so high. In most observations, the higher end of the m^{-3} range cannot be detected because of limitation in vertical resolution and/or in observable height range. According to a temperature m spectrum observed by radiosondes shown in Fig. 9a in Sato and Yamada (1994), the higher end of the steep-slope range is observed at ~6×10^{-2} rad m^{-1} (vertical wavelength of ~100 m). By intercomparing GW spectra simulated by several convection-permitting models, Stephan et al. (2019) showed that model-simulated spectra also have steep slopes in a high m range similar to observations.

Several theories have been developed regarding these characteristic m spectra. Adopting a concept of superposition of saturated GWs, Smith et al. (1987) developed a theoretical model that explains that the horizontal wind spectrum is described as

$N^2/6m^3$ for $m \gtrsim m_*$, where N is the buoyancy (Brunt–Väisälä) frequency. They assumed that the spectral range occupied by a single saturated GW (Δm) is proportional to m (Dewan & Good, 1986). Sato and Yamada (1994) considered the change in m of a single saturated GW in the linear vertical shear $\mathrm{d}U/\mathrm{d}z$ of the background wind parallel to the horizontal wavenumber vector and derived a theoretical spectrum without the assumption of $\Delta m \propto m$. The spectral form of the horizontal wind fluctuations shown by Sato and Yamada (1994) is expressed as follows:

$$P_u(m) \approx N^2 \cdot (2m^3 \cdot \Delta z |dU/dz|)^{-1} \sqrt{N^2/m^2 + f^2/k^2}, \tag{1}$$

where Δz is the height expanse for the spectrum calculation, k is the horizontal wavenumber, and f is the Coriolis parameter. This spectral theory succeeded in explaining the characteristic shape and level of the m spectra. However, it has not been fully confirmed that the observed m spectra are totally attributable to GWs. A useful approach to examine this issue is to calculate GW m spectra by extracting GWs as fluctuations having high total horizontal wavenumbers using a recently available GW-permitting general circulation model (GCM).

The theories describing the m spectra give the basis of nonorographic GW parameterizations (e.g., Hines, 1997a, 1997b; Warner & McIntyre, 1996, 1999) used widely in climate models. Descriptions of vertical and horizontal variations of GW spectra in a GW-permitting model may provide useful guidelines for the GW parameterizations (e.g., McLandress & Scinocca, 2005; Watanabe, 2008).

In this study, we use outputs from a hindcast of December 2018 using a GW-permitting GCM extending from the surface to the lower thermosphere (Okui et al., 2021). Fluctuations having total horizontal wavenumbers of 21–639 are designated as GWs. First, it is verified that the model reproduces the main observed spectral properties. Next, to examine the contribution of GWs to the spectra in the m^{-3} range, m spectra of GWs and all-fluctuation components obtained from each single profile, just as they would be extracted from radar or radiosonde observations, are compared. Global distributions of parameters describing the characteristics of GW spectra are also examined for each height region in the middle atmosphere. The remainder of this paper is structured as follows. Detailed descriptions of the model and the analysis method are given in Section 2. Results are discussed in Section 3. A summary and concluding remarks are presented in Section 4.

2 Method and Model Description

The model used in this study is a high-resolution version of the Japanese Atmospheric GCM for Upper Atmosphere Research (JAGUAR) (Watanabe & Miyahara, 2009). This model comprises 340 vertical layers from the surface to the geopotential height of ~150 km, with a log-pressure height interval of 300 m throughout the middle atmosphere, and it has a horizontal-triangularly truncated spectral resolution of T639, whose minimum resolvable horizontal wavelength is ~60 km. No parameterizations for subgrid-scale GWs were used in the present study. It is considered that the JAGUAR, whose vertical grid interval is 300 m, realistically resolves GWs having wavelengths at least longer than ~2.0 km (6–7 grids). By performing GCM simulations with different vertical resolutions (Δz), Watanabe et al. (2015) examined the dependence of GW momentum flux on the vertical resolution, suggesting that the vertical grid interval shorter than or equal to 300 m give almost the same amount of the fluxes. This fact suggests that the GWs having the most part of momentum fluxes can be resolved with Δz= 300 m, which supports the validity of using a GCM having a vertical resolution of 300 m to examine characteristics of GW m spectra.

A hindcast was performed for 5 December 2018 to 17 January 2019 using global analysis data produced by the JAGUAR–Data Assimilation System (JAGUAR-DAS) (Koshin et al., 2020, 2022) in a medium-resolution (T42L124) version of the JAGUAR as initial data. A four-dimensional local ensemble transform Kalman filter and a filter called incremental analysis updates (Bloom et al., 1996) are used in the JAGUAR-DAS. The PrepBUFR observational dataset provided by the National Centers for Environmental Prediction (NCEP), satellite temperature data from the Aura Microwave Limb Sounder (MLS) and the Sounding of the Atmosphere using Broadband Emission Radiometry (SABER) on the Thermosphere, Ionosphere, Mesosphere Energetics Dynamics (TIMED) satellite, and brightness temperature data from the Special Sensor Microwave Imager/Sounder (SSMIS) were assimilated. The hindcast period was divided into consecutive 4-day intervals, for each of which an independent run was performed using the high-resolution JAGUAR. Each model run consisted of a spectral nudging run over 3 days and a free run over the subsequent 4 days. We analyzed the outputs at 1-hour intervals from the 4-day free runs only for the 5–20 December 2018. We did not use data from later periods because substantial modulation of GW fields was expected in association with the onset of major sudden stratospheric warming on 1 January 2019. Detailed analysis of this sudden stratospheric warming is presented in Okui et al. (2021).

In the present study, GWs were extracted as fluctuations having total horizontal wavenumbers of 21–639 (horizontal wavelengths of λ_h< 2000 km). We did not use any vertical filter for extraction of GWs. Note that some GWs may have longer horizontal wavelengths than this cutoff wavelength (e.g., Chen et al., 2013, 2016; Chen and Chu, 2017). However, several radiosonde and radar observations showed that dominant horizontal wavelengths of GWs in the lower stratosphere are hundreds of kilometers except at low latitudes, where they can be ~1000 km or longer (e.g., Sato, 1994; Wang et al., 2005). Analyzing satellite observation data, Ern et al. (2018) showed that dominant horizontal wavelengths of GWs in the stratosphere and mesosphere along the satellite orbit, which would always overestimate their true values, are 500–2000 km. Based on these results from previous studies, we chose ~2000 km as the cutoff wavelength.

To imitate the extraction methods of fluctuations in radar and radiosonde observations, in addition to GW spectra, we calculated m spectra for fluctuations with all horizontal wavenumbers using vertical profiles in which only linear trends in the vertical were removed. Hereafter, these profiles are referred to as “all fluctuations”. It is possible that all fluctuations include not only GWs but also vertical variations of larger-scale waves, such as Rossby waves and equatorial waves, and mean fields. Comparison between the m spectra of GWs and all fluctuations allows us to examine the GW contribution to observed m spectra by radars, lidars, and radiosondes. Temperature fluctuations were multiplied by g/T_0N, where T_0 is the background temperature extracted as a linear trend from each unfiltered temperature profile, and g is gravitational acceleration. Because the obtained power spectra are expected to have steep slopes, i.e., proportional to $\sim m^{-3}$, prewhitening and recoloring processes were performed before and after the calculation of spectra, respectively (e.g., Sato et al. 2003). The degree of prewhitening β was taken as 0.95 in this study. Profiles having finite data length were tapered using a 10% cosine-tapered window for the first and last tenth of the data series. Using a Fast Fourier Transform, power spectra were calculated from these processed profiles of GWs (i.e., components with n= 21–639) and all fluctuations. The spectra calculated in this way were multiplied by an energy correction factor of 1/0.875 to compensate the spectral reduction due to the 10 % cosine-tapered window.

3 Results and Discussion

3.1 Contribution of GWs to m^{-3} spectra

The zonal wind, meridional wind, and temperature spectra from 5–20 December 2018 at Shigaraki (35°N, 136°E), Japan, where the MU radar is located, are shown in Fig.

1. Figs. 1a–c are spectra in the lower stratosphere and Figs. 1d–f are those in the middle and upper mesosphere, for which the m spectra from the MU radar observations were reported by Tsuda et al. (1989). The height regions for the spectra were determined such that N^2 is approximately constant, as assumed in Smith et al. (1987). Note that the MU radar observation shown by Tsuda et al. (1989) were consistent with the theory of Smith et al. (1987).

It is important that the model-simulated spectra of all fluctuations have a shape with a steep slope of $\sim m^{-3}$ in the high m range in both the lower stratosphere and the mesosphere. This feature is consistent with the spectra calculated from MU radar observations (e.g., Tsuda et al., 1989). The $\sim m^{-3}$ range of the spectra is in good agreement with the theoretical spectral model derived by Smith et al. (1987). The GW spectra are bent at a specific value of m of 3–5 × 10^{-4} m^{-1} (a vertical wavelength λ_z of ~2–3 km) in the lower stratosphere and 1–2 × 10^{-4} m^{-1} (λ_z= ~5–10 km) in the mesosphere. In the m range above the bending point, the GW spectra are nearly proportional to m^{-3} and they agree well with the spectra of all fluctuations. However, at lower ms, the spectral density of the GW spectra is smaller than that of all fluctuations, even within the $\sim m^{-3}$ range of the all-fluctuation spectra. These facts suggest that the observed spectral slopes of $\sim m^{-3}$ mainly consist of GWs in the high m range, but that disturbances other than GWs also contribute substantially to the spectra at lower m part of the $\sim m^{-3}$ range. The highest m in the range where there is notable disagreement between the spectra of GWs and those of all fluctuations is lower in the mesosphere than in the lower stratosphere. This difference shows that GWs having longer vertical wavelengths are dominant in the mesosphere than in the stratosphere.

A series of meridional wind spectra in the middle stratosphere for z= 18–25 km, averaged over the latitudinal range of ±5° around each latitude, are shown in Fig. 1g. To compare them with observed spectra, we chose the same height region as Sato et al. (2003), in which the m spectra were obtained as a function of the latitude using radiosonde observations performed over a research vessel for the middle Pacific. To estimate the parameters describing the characteristics of these spectra, the obtained spectral curves were fitted to the following equation (Allen & Vincent, 1995) using a trust-region algorithm (Conn et al., 2000):

$$P_{\mathrm{ALL}}(m) = F_0 \frac{m/m_*}{1 + (m/m_*)^{t+1}}, \quad P_{\mathrm{GW}}(m) = F_0 \frac{m/m_{\mathrm{g}*}}{1 + \left(m/m_{\mathrm{g}*}\right)^{t+1}}, \qquad \text{(2a, 2b)}$$

where m_* in Eq. (2a) and $m_{\mathrm{g}*}$ in Eq. (2b) are the characteristic wavenumbers (approximate bending wavenumbers) of an all-fluctuation spectrum $P_{\mathrm{ALL}}(m)$ and the

GW spectrum $P_{\mathrm{GW}}(m)$, respectively; F_0 is a parameter representing the amplitude at $m = m_*$ or $m_{\mathrm{g}*}$; and t represents the spectral slope of opposite sign. The closed (open) circles in Fig. 1g represent $m_{\mathrm{g}*}$ (m_*) estimated for each spectrum.

The spectra at latitudes of 25° S–25° N have shape with an ~m^{-3} slope at a higher m range. However, the spectral slopes at higher latitudes are relatively gentle and almost proportional to ~m^{-2}, even in the high m range. This feature of steeper spectral slope at lower latitudes is consistent with the observations by Sato et al. (2003). Similar to the comparison with the MU radar observations at Shigaraki (Figs. 1a–f), the difference in spectral density between the GWs and all fluctuations is substantial at $m < m_{\mathrm{g}*}$ except at 45°–75° S and 45°–75° N, where GWs are dominant, even in a low m range. The difference is particularly large at low latitudes of 25° S–25° N and in the polar regions at 85° S and 85° N. The folding wavenumber for the all-fluctuation spectra is slightly (~1.1–2 times) smaller than $m_{\mathrm{g}*}$ at 25° S–25° N.

It is considered that the contribution of equatorial waves to the spectral densities is large at low latitudes near the equator. Because meridional wind fluctuations are examined here, waves except Kelvin waves are possible candidates. However, typical meridional scale of equatorial waves such as Rossby-gravity waves and equatorial inertia-gravity waves is ~1500 km (~7° S–7° N). Therefore, these waves hardly account for the additional spectral density at 25° S and 25° N. Inertial instability is another possible candidate for the meridional wind structure having a vertical wavenumber of ~1–2 × 10^{-4} m^{-1} corresponding a vertical wavelength of ~10 km (e.g., Dunkerton, 1981; Rapp et al., 2018; Strube et al., 2020). However, anomalous potential vorticity, which is the inertially unstable condition, is rarely observed in the region of z = 18–25 km in the analyzed model data (not shown). Secondary circulation associated with the QBO has a larger vertical scale than the range of m^{-1} discussed here. The cause of the differences between GW and all-fluctuation spectra at low latitudes is left for future studies. As for the spectra at 85° S and 85° N, the difficulty in handling zonal and meridional wind fluctuations near the poles may have affected the results. Since it may be useful for comparison with lidar and radar observations in the future, zonal mean and ±5° latitude mean v spectra for z= 30–60 km and 80–100 km are shown in Fig. S1 in Supporting Information.

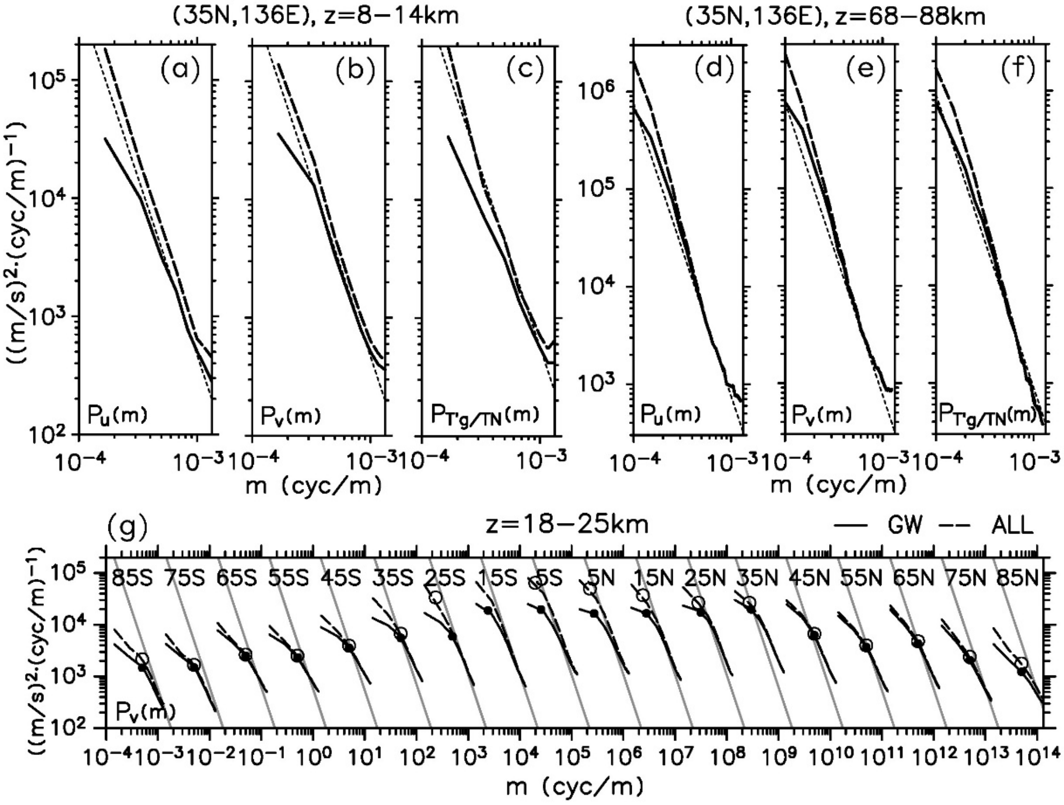

Figure 1 Vertical wavenumber spectra from 5–20 December 2018 of (a, d) zonal wind, (b, e) meridional wind, and (c, f) temperature fluctuations at Shigaraki (35° N, 136° E), Japan, in the height regions of (a–c) z= 8–14 and (d–f) 68–88 km. Solid and dashed curves show the spectra of GWs and all-fluctuation components, respectively. Theoretical spectra from Smith et al. (1987) are indicated by thin dotted lines. (g) Meridional wind spectra from 5–20 December 2018 for z=18–25 km averaged zonally and over the respective latitude regions of ±5° of the center of the latitudes shown in the figure. Closed (open) circles indicate the folding point of GW (all-fluctuation) spectra. Gray lines are the theoretical spectra from Smith et al. (1987). The scale of the horizontal axis is for the spectra at 85° S and curves for the other latitudes are shifted by an order of magnitude one by one.

3.2 Characteristics of GW spectra in the middle atmosphere

To examine the behavior of GWs in the middle atmosphere, the vertical and geographical distributions of parameters m_{g*}, F_0, and t in Eq. (2b) were estimated for $P_{GW}(m)$. Figure 2 shows the zonally averaged parameters at each height region as functions of latitude. The height regions used for calculation were determined such that

N^2 was almost constant in each region. The main features of the parameter distributions for the zonal wind spectra (Figs. 2a–c), meridional wind spectra (Figs. 2d–f), and temperature spectra (Figs. 2g–i) are generally consistent. The following discussion is based on the parameters of meridional wind spectra, but similar results were obtained for both the zonal wind and the temperature spectra.

The characteristic wavenumber m_{g*} is lower at higher altitudes (Fig. 2a). This is consistent with the theoretical expectation of Smith et al. (1987). For z= 60–90 km in the middle and upper mesosphere, m_{g*} are 1/3–2/3 of those in the lower stratosphere (z= 18–33 km). Parameter F_0 is larger in higher altitude regions (Fig. 2c). The values of F_0 for z= 60–90 km are 50–200 times larger than those for z= 18–33 km. Adopting the concepts of wave amplitude growth with height and GW saturation, it is theoretically estimated that the ratio of m_{g*} for z= 60–90 km to that for z= 18–33 km is ~1/6–1/3, and that the ratio of F_0 for z= 60–90 km to that for z= 18–33 km is ~40–240 (Smith et al., 1987). The model results roughly agree with these theoretical estimates. Thus, the vertical variations of the parameters are mostly explained by growth in the amplitude of saturated GWs due to the exponential decrease in atmospheric density. However, vertical variation in m_{g*} is slightly more moderate than that of the theoretical estimates. One possible explanation for the departure from the theory is that the assumption of GW saturation is not necessarily fulfilled. In the low-latitude region of 15° S–25° N, t is ~2.5 and approximately constant with height. At mid- and high latitudes, t is 1.5–1.8 for z= 18–33 km and approaches ~3 with height. This wide distribution of t is consistent with Lidar observations at McMurdo, Antarctica (78° S, 167° E) (Lu et al., 2015; Zhao et al., 2017; Chu et al., 2018) and at Urbana (40° N, 88° W) (Senft & Gardner, 1991).

In terms of latitudinal variation, m_{g*} has a maximum value of 2.2–2.5 × 10^{-4} m^{-1} at 20° S–40° N in the lower and middle stratosphere (i.e., z= 18–33 km and z= 33–45 km, respectively). It is almost homogeneous in the uppermost stratosphere and mesosphere (z= 45–60 km and z= 60–90 km, respectively). The value of t shows large latitudinal variations. For z= 45–60 km in the uppermost stratosphere and lowermost mesosphere, t has two significant peaks of ~2.7 at ~15° S and ~3.0 at ~50° N. It is expected that GWs tend to be saturated in a high m range in regions of weak background wind. However, the spectra may not be due to saturated GWs below and near the strong eastward or westward jet in the middle atmosphere, since intrinsic phase velocity becomes large due to the Doppler shift and thus m becomes small in a strong background wind. Below the jets, the spectral slopes are highly affected by the strong vertical shear. Due to its m dependency, this shear effect steepens GW spectra (see Section 3.3). At 50° N, t

increases with height from ~1.8 in the lower stratosphere (i.e., z= 18–33 km), which is much smaller than 3, to ~3.0 in the height region of 45–60 km, where the eastward jet core is located. The shear effect on GW spectra below the jet core also prevents GW saturation, which is discussed in detail in Section 3.3. This difference in the factors controlling GW spectral slopes t among different latitudes is a possible reason for the large latitudinal variation in t.

As for the F_0 distribution, there are two peaks of ~3 × 10^4 m^3 s^{-2} at ~15° S and ~4 × 10^4 m^3 s^{-2} at 50°–75° N in the lower stratosphere (z= 18–33 km). The former peak at ~15° S shifts to higher latitudes at higher altitudes, as is consistent with the poleward propagation of eastward GWs due to refraction toward the summer westward jet (e.g., Sato et al., 2009). The latter peak in the Northern Hemisphere (NH) corresponds to the region near the eastward jet in the middle atmosphere. This peak is sharpest at ~55° N in the region of z= 45–60 km, where the jet core exists, and spreads over a broader latitude region in the region of z= 60–90 km above the jet. These sharpening and broadening may be a result of lateral propagation of GWs from their source.

Note that the F_0 peak at northern mid- and high latitudes observed for z= 18–33 km in Fig. 2f is not clear in the spectra for z= 18–25 km shown in Fig. 1g. This apparent inconsistence in lower-stratospheric GW spectra between the two height regions is likely due to the difference in the background wind condition. The height region of 18–25 km corresponds to the region far below the middle atmosphere eastward jet, while the region of z= 18–33 km includes the lower part of the jet. In the eastward jet region, it is considered that GWs tend to have longer vertical wavelengths, which makes a steep spectral slope extend toward lower m and thus F_0 larger. Spectra averaged zonally and over a latitudinal region of $\pm 5°$ for z= 18–33 km showed better consistency with F_0 in Fig. 2f (not shown).

Figure 3 illustrates horizontal maps of m_{g*}, t, and F_0 for z= 18–33 km in the lower stratosphere. The contours represent zonal wind. In the high-latitude region of the NH, m_{g*} is small along the eastward jet. This small m_{g*} can be explained by the Doppler shift in the jet as follows. The ground-based phase velocity of a GW c is conserved in the background field that is steady and homogeneous in the horizontal wavenumber vector direction. However, the intrinsic phase velocity $\hat{c}$ ($\equiv c - U$, where U denotes background horizontal wind) varies when U changes in the vertical. Above a weak-wind layer near z= 20 km, the background zonal wind U has an eastward vertical shear below the NH middle atmosphere jet core. On the other hand, a major part of GWs reaching the weak-wind layer near z= 20 km should have small or westward c because they need to pass through the tropospheric eastward jet below. Thus, the intrinsic phase velocity $\hat{c}$ of the GWs near the weak wind layer is westward and becomes larger while they propagate upward in the eastward shear below the middle atmosphere jet core due to the Doppler shift. The linear gravity wave theory indicates that stronger U makes m smaller, because $m^2 \approx N^2/(c-U)^2$. Thus, m_{g*} near the eastward jet is expected to get small.

In contrast, in the low-latitude region, especially 20° S–10° N, both m_{g*} and t are large. This feature can be attributable to a zero-wind phase of the QBO over a latitude region of 15° S–15° N (not shown). Assuming that c is small, in the background condition of small $U, \hat{c}$ $(= c - U)$ is small, m is large, and the saturation condition $|\hat{c}| = |u'|$, where $|u'|$ is the horizonal wind amplitude of the GW, easily holds. It is worth noting that the geographical distribution of m_{g*} is consistent (i.e., has negative correlation) with the satellite observations for dominant GW vertical wavelengths shown by Ern et al. (2018). There are F_0 peaks along the middle atmosphere jet in the Northern Hemisphere, at low latitudes in the Southern Hemisphere, and around South America. Such geographical distribution of the F_0 peaks is also roughly consistent with that of the GW amplitude peaks observed by satellites shown by Ern et al. (2018). Sato et al. (2009) suggested that steep mountains, jet-front systems in winter, and subtropical monsoon convection in summer are dominant GW sources. The distribution of such GW sources are likely responsible to the observed F_0 peaks.

Maps of the spectral parameters in the uppermost stratosphere and lowermost mesosphere (i.e., z= 45–60 km) are shown in Fig. 4. Interestingly, t in the eastward jet region in the Northern Hemisphere is notably large, ranging from 3–3.75. At low latitudes in the Southern Hemisphere, t is also relatively large along the westward jet. As mentioned above, the m of a GW becomes small where U is strong. Because $N^2/m^2 \gg f^2/k^2$ in Eq. (1) derived by Sato and Yamada (1994), which is a theoretical saturated spectrum of a GW propagating in linear wind shear, the spectral slope approaches −4. The distributions of m_{g*} and F_0 in the lower mesosphere (Figs. 4a and 4c, respectively) have less spatial variability than those in the lower stratosphere (Figs. 3a and 3c, respectively). This spatial uniformity was also observed in the height region of 60–90 km in the middle and upper mesosphere (not shown).

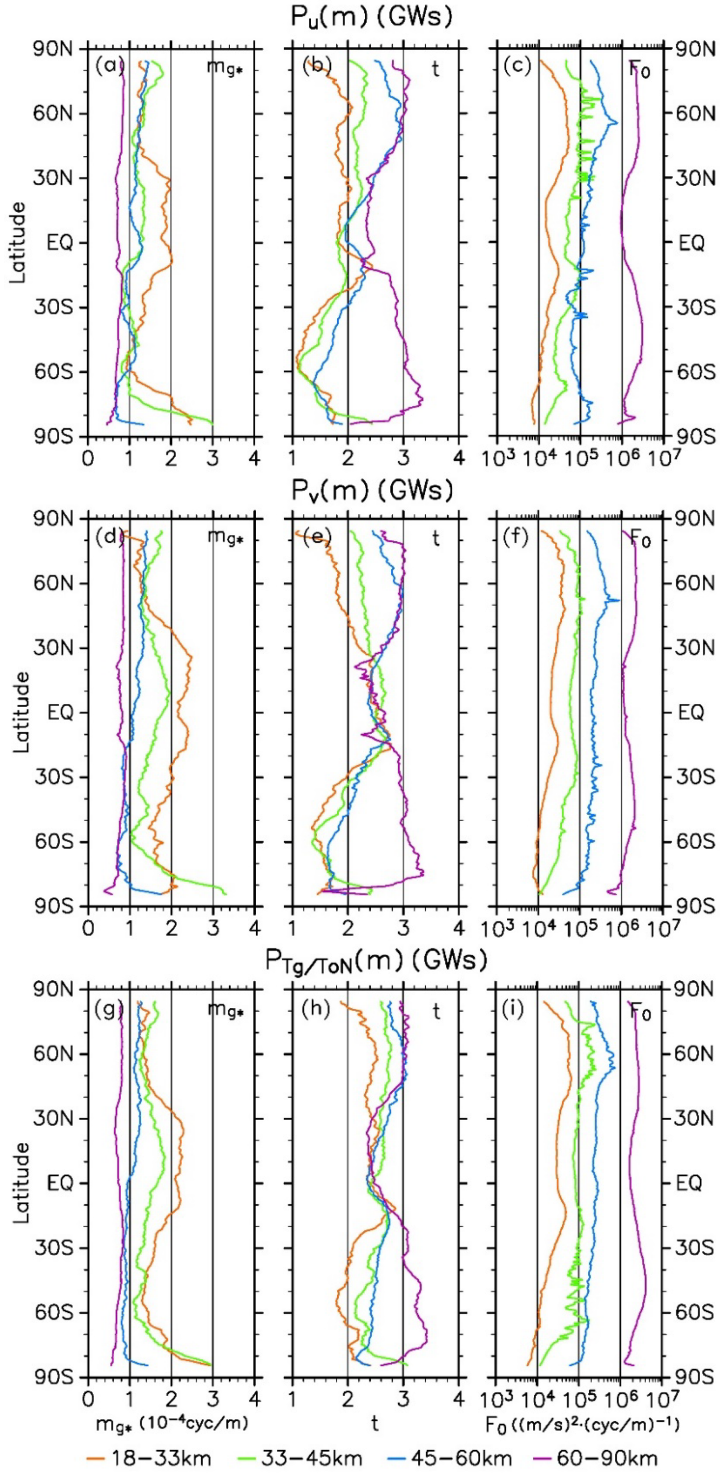

Figure 2 Zonal mean m_{g*}, t, and F_0 of (a–c) zonal wind, (d–f) meridional wind, and (g–i) temperature spectra of GWs from 5–20 December 2018 as functions of latitude. The color of the curves represents the height region: z= 18–33 km (orange), 33–45 km (green), 45–60 km (blue), and 60–90 km (purple).

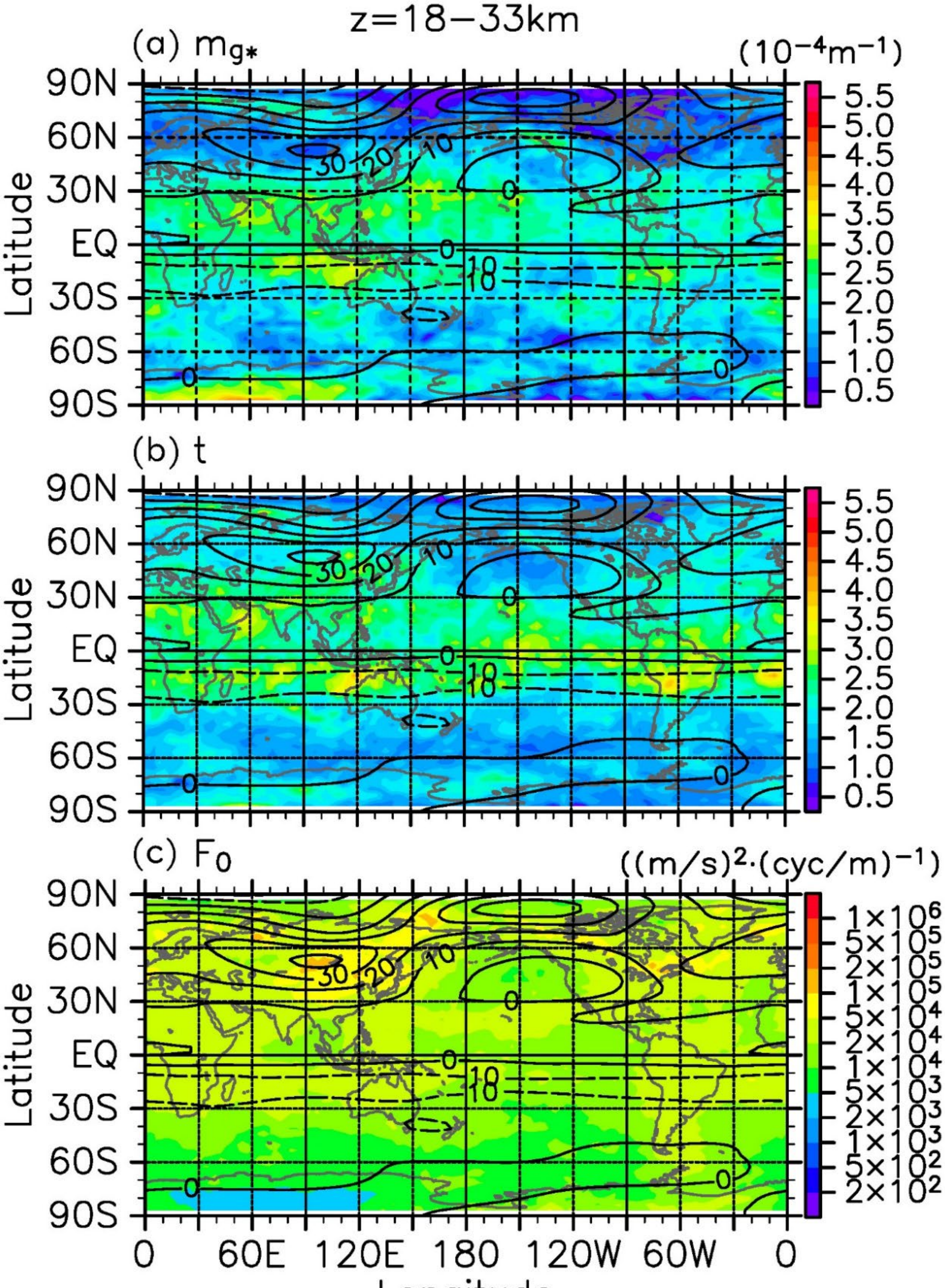

Figure 3 Maps of (a) m_{g*}, (b) t, and (c) F_0 for meridional wind spectra of GWs in the lower stratosphere for z= 18–30 km from 5–20 December 2018. Contours show zonal wind.

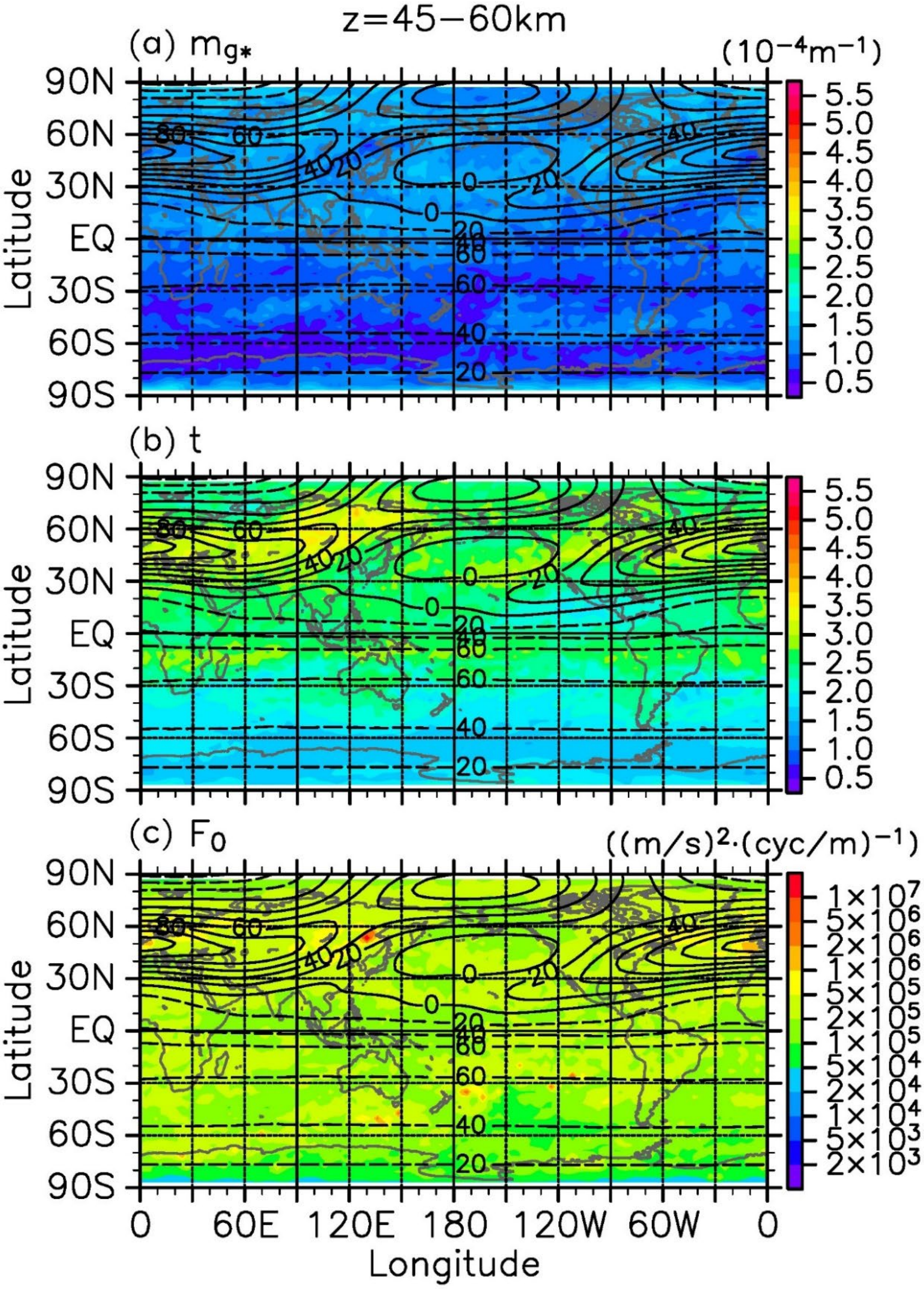

Figure 4 Similar to Fig. 3 but for the uppermost stratosphere and lowermost mesosphere for z= 45–60 km from 5–20 December 2018. Note that the colormap used in Fig. 4c and the contour interval are different from those used in Fig. 3d.

3.3 Shear effect on vertical variation of GW spectra

At mid- and high latitudes below the height region of 45–60 km, the spectral slope becomes steeper with height (Figs. 2b and 2e). Additionally, the decrease in m_{g*} with height is much more modest than that at low latitudes (Figs. 2a and 2d). These characteristic vertical changes of the spectral parameters (i.e., increase in t and modest decrease in m_{g*} with height) at mid- and high latitudes at z< 60 km is particularly remarkable near the middle atmosphere eastward and westward jets (Fig. 4). Here, the effect of strong vertical shear below the jets on the shape of a GW spectrum is examined.

Consider a GW propagating in a background wind $U(z)$ that is parallel to the horizontal wavevector and varies only in the vertical. The dispersion relation for a hydrostatic and nonrotational internal GW is as follows (e.g., Andrews et al., 1987; Fritts & Alexander, 2003):

$$\widehat{\omega}^2 = \frac{k^2 N^2}{m^2}, \tag{3}$$

where $\widehat{\omega}$ is the intrinsic frequency and k is the horizontal wavenumber. We can take the sign of $\widehat{\omega}$ as positive without loss of generality. Under this setting, m is negative for a GW having an upward group velocity. Thus, based on the Wentzel–Kramers–Brillouin approximation, the variation of $m = m(U;z)$ is described as follows:

$$m(U;z) = -\frac{N}{|c - U(z)|}. \tag{4}$$

This equation yields the z derivative of $m(U;z)$:

$$\frac{\mathrm{d}m}{\mathrm{d}z}\left(= -\frac{\mathrm{d}|m|}{\mathrm{d}z}\right) = \frac{\mathrm{d}m}{\mathrm{d}U}\frac{\mathrm{d}U}{\mathrm{d}z} = \frac{m^2}{N}\frac{U - c}{|U - c|}\frac{\mathrm{d}U}{\mathrm{d}z}. \tag{5}$$

Here, we assume that dominant GWs have westward intrinsic phase velocities $\hat{c}$ in the middle atmosphere eastward jet, i.e., $|U - c| = U - c$, as before. In the summer hemisphere, there is a wind-reversal layer between the eastward jet in the troposphere and westward jet in the middle atmosphere. Convection at low latitudes (e.g., Sato et al., 2009) and shear instability just above the tropospheric jet (e.g., Bühler et al., 1999; Okui & Sato, 2020) are possible sources of GWs, which generally have eastward $\hat{c}$ $(= c - U)$ in the middle atmosphere westward jet. Thus, both $U - c$ and $\mathrm{d}U/\mathrm{d}z$ are positive (negative) below the middle atmosphere eastward (westward) jet. The rightmost side of the Eq. (5) is positive and hence $\mathrm{d}m/\mathrm{d}z$ is larger for higher $|m|$. This fact shows that the absolute wavenumber $|m|$ decreases more rapidly with height in a higher $|m|$ range. In addition, the horizontal wind amplitude $|u'|$ is modulated by the modulation of m assuming the momentum flux conservation:

$$|u'|^2 = \left|\frac{m}{k}\right| |u'w'| \propto |m|. \tag{6}$$

Both changes in m and in $|u'|$ shown in Eqs. (5) and (6) by the vertical shear below the peak of a jet acts to increase in t for the GW spectra.

To evaluate the shear effect on a spectral shape quantitatively, we obtain theoretical spectra by integrating Eq. (5) numerically in the vertical for the zonal wind u' spectra of GWs at 50°–60° N around the middle atmosphere eastward jet and at 50°–60° S around the westward jet. We take the representative heights $z_{\mathrm{r}i}$ (i=1, …, 4), whose definition is described below, as the upper and lower limits for the integration. Here, i denotes each of four height regions in which the model-simulated spectra were calculated (i.e., z= 18–33 km, 33–45 km, 45–60 km, and 60–90 km). The height $z_{\mathrm{r}i}$ is defined as the average height weighted by the product of $u'(z)^2$ and 10% cosine-tapered window, taking a possible large vertical dependence of the GW amplitudes into account. We took z_{r1}= 25.47 km for z= 18–33 km, z_{r2}= 40.01 km for z= 33–45 km, z_{r3}= 54.30 km for z= 45–60 km, and z_{r4}= 73.86 km for z= 60–90 km for 50°–60° N, and z_{r1}= 24.98 km for z= 18–33 km, z_{r2}= 39.80 km for z= 33–45 km, z_{r3}= 53.46 km for z= 45–60 km, and z_{r4}= 81.41 km for z= 60–90 km for 50°–60° S. We also consider the wave saturation using the theory by Smith et al. (1987).

Detailed calculation steps are as follows: (i) The model-simulated spectra for z= 18–33 km are used for initial values. The initial heights for the integration were chosen as z_{r1}= 25.47 km for 50°–60° N and 24.98 km for 50°–60° S. Background zonal wind U was derived by averaging a zonal wind profile zonally and over the respective latitude region. Following steps (ii)-(iv) are repeated for the three height regions of i=2–4 from below. (ii) By numerically integrating Eq. (5) from $z_{\mathrm{r}i-1}$ to $z_{\mathrm{r}i}$ (i=2–4) for each height region, m was updated. (iii) At each step of the m integral, amplitude growth due to decrease in atmospheric density at higher altitudes was included for the spectral density using Eq. (16) of Smith et al. (1987), i.e., $P(m) \propto e^{z/(2H_{\mathrm{E}}/3)}$, where H_{E} ranges from 14–21 km. Here, we took 18 km for the value of H_{E}. In addition, the spectral density at each m is multiplied by the ratio of two ms before and after the m-integral step considering Eq. (6). (iv) When an integrated spectrum exceeds the spectral density of the theoretical spectrum of Smith et al. (1987) (i.e., $N^2/12m^3$) in a specific m range, we regarded GWs in this m range as saturated and replaced the spectral density with that of the Smith et al. (1987)'s theoretical spectrum.

The results are shown in Fig. 5. The profile of the background zonal wind U in each latitude region is plotted in Figs. 5a and 5e. The spectra obtained by the above calculation are denoted by black curves in Figs. 5c and 5g, which are overlayed on the model-simulated spectra denoted by colored curves (same as in Figs. 5b and 5f). Note that m for the horizontal axes means $|m|$. Each black curve indicates the result at z_{ri}. The results of the calculation without the shear effect on m are shown in Figs. 5d and 5h for comparison. The light-colored curves in Figs. 5b and 5f indicate theoretical spectra of Smith et al. (1987). The dashed curves show the spectra without the treatment of wave saturation (i.e., without the step (iv) in the previous paragraph).

For both latitude regions, the estimated spectra with shear effect (Figs. 5c and 5g) accord better with the model-simulated spectra than the spectra estimated without shear effect (Figs. 5d and 5h). This accordance of the estimated spectra with shear effect is especially significant for z= 33–45 km at 50°–60° N, and z= 33–45 km and 45–60 km at 60°–50° S. However, there are a few exceptions. In the uppermost stratosphere and lowermost mesosphere (z= 45–60 km) at 50°–60° N, the estimated spectral density with shear effect is ~1.5 times smaller than the model-simulated spectral density (denoted by the blue curve). The estimated spectral density was calculated based on the assumption that GWs propagate only vertically. In-situ generation from the eastward jet in the middle atmosphere and/or lateral propagation toward the jet (e.g., Sato et al., 2009, 2012) give possible explanation for the difference between the model-simulated spectrum and the estimated spectrum in the region of z= 45–60 km at 50°–60° N.

Even in the m range where the wave-saturation threshold is not fulfilled (i.e., without dashed curves), these estimates of shear-affected spectra show the increase in spectral slope that is also seen in the model-simulated spectra. The most interesting suggestion obtained from this simple investigation is that the steep slope of the GW m spectrum is likely formed by strong vertical shear, even in the absence of wave saturation. In contrast, the resultant spectral densities for z= 60–90 km exceed the Smith et al. (1987)'s one at almost all ms as shown in Fig. 5 for both the 50°–60° N and 60°–50° S cases, regardless of whether the shear effect was taken into account or not. In these regions, it is considered that wave saturation is the main cause of the steep spectral slope.

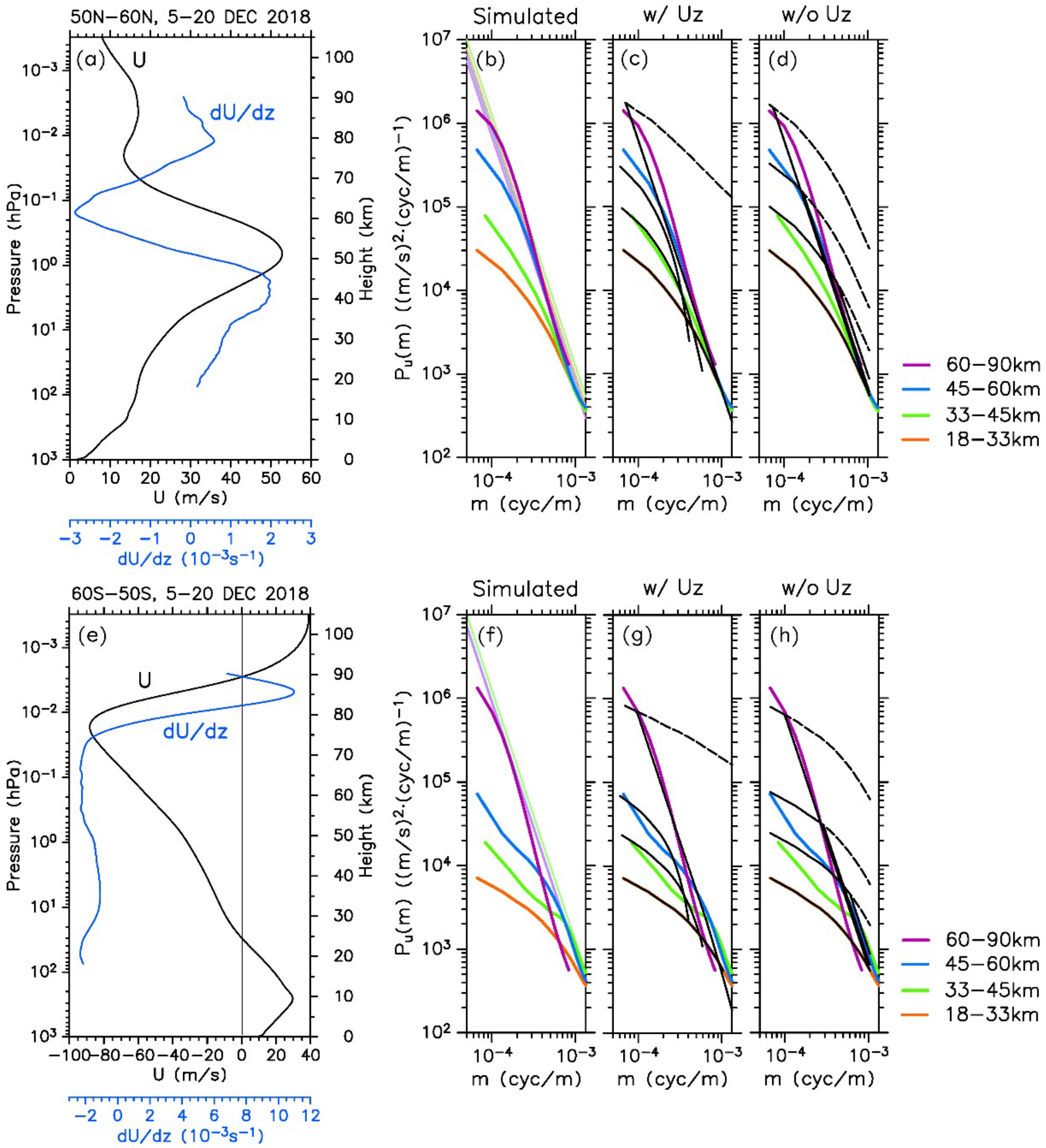

Figure 5 Estimates of the shear effect on GW spectra at (a–d) 50°–60° N and (e–h) 60°–50° S from 5–20 December 2018. (a, e) Vertical profiles of background zonal winds U averaged zonally and over the shown latitude regions. Blue curves represent $\mathrm{d}U/\mathrm{d}z$, which was used for the calculation. (b, f) Model-simulated spectra (colored curves; legends are shown on the right). Curves with the same but lighter colors show theoretical spectra (Smith et al., 1987), which almost overlap with each other. (c, g) Estimated spectra with shear effect (black curves). (d, h) Estimated spectra without shear effect (black curves). These spectra are overlayed on the model-simulated spectra in the respective height regions. Dashed curves represent the results with wave saturation effect ignored.

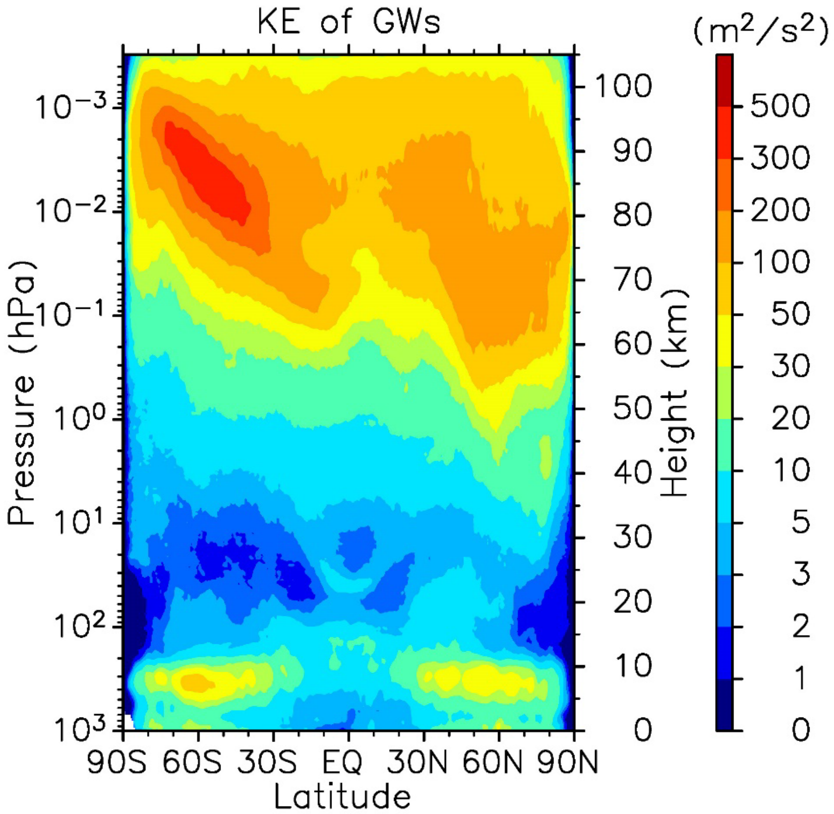

Figure 6 Latitude-height section of zonal mean kinetic energy of GWs from 5–20 December 2018.

4 Summary and Concluding Remarks

Using the output of a hindcast of the middle atmosphere in December 2018 performed by a GW-permitting high-top GCM, we examined the contribution of GWs to the universal vertical wavenumber ($\sim m^{-3}$) spectra. The results of this study are as follows.

1. Model-simulated spectra in the stratosphere and mesosphere have shape with a steep slope of $\sim m^{-3}$ in a high m range, consistent with observations shown by previous studies.

2. In most regions of the middle atmosphere, GWs do not contribute to the entire steep-slope part of the m spectra obtained by the previous observational studies. GWs make a dominant contribution to the m spectra only in a high m part of the steep-slope range. Disturbances other than GWs also contribute to the spectra in its low m part.

3. The lowest end of the m spectral range in which GWs are dominant is lower in

the mesosphere than in the stratosphere.

4. Contribution of the disturbances other than GWs is especially large in equatorial and polar regions.

Parameters describing the characteristics of GW spectra were also examined. The m_{g*} value of GW spectra is lower at higher altitudes. The spectral density at m_{g*} (i.e., $F_0/2$) is larger at higher altitudes. These vertical variations are consistent with wave saturation and the exponential decrease in density. Parameter t increases with height and approaches ~3 in mid- and high-latitude regions. In general, t is not necessarily ~3 (i.e., $\sim m^{-3}$), which is consistent with several previous studies (e.g., Sato et al. 2003; Lu et al. 2015). The spectral slope in the high m range is steeper than that in the low m range. In the lower stratosphere, the geographical distribution of F_0 is roughly consistent with the observations reported in previous studies. We also examined the shear effect on GW spectra below the eastward and westward jets in the middle atmosphere. The results showed that strong vertical shear, in addition to wave saturation, is significantly responsible for making the slope of the GW spectra steeper.

It is expected that the characteristics of m spectra have seasonal and interannual variations following different background conditions such as the QBO in the equatorial region, for example. To examine the universality of the results, it would be useful to perform similar simulations for other seasons and different years. The JAGUAR hindcasts, containing three-dimensional and global data of GWs in the middle atmosphere, is a strong tool for quantitative elucidation of GW behavior in the middle atmosphere.

Acknowledgments

All figures in this paper were created using the Dennou Club Library (DCL). This study benefitted from stimulating discussions at the International Space Science Institute (ISSI) Gravity Wave activity. The study was supported by JST CREST (grant JPMJCR1663) and JSPS KAKENHI (grant JP21J20798). The hindcasts were performed using the Earth Simulator at the Japan Agency for Marine-Earth Science and Technology (JAMSTEC). The processed model data are available at the following website: https://pansy.eps.s.u-tokyo.ac.jp/archive_data/Okui_etal_GW-spectra/. We thank James Buxton, MSc, from Edanz (https://jp.edanz.com/ac) for editing a draft of this manuscript.

References

Andrews, D.G., Holton, J.R., & Leovy, C.B. (1987). *Middle Atmosphere Dynamics*. San Diego, CA: Academic Press.

Allen, S. J., & Vincent, A. (1995). Gravity wave activity in the lower atmosphere: Seasonal and latitudinal variations. *Journal of Geophysical Research*, **100**, 1327–1350. https://doi.org/10.1029/94JD02688

Bloom, S. C., Takacs, L. L., DaSilva, A. M., & Levina, D. (1996). Data assimilation using incremental analysis updates. *Monthly Weather Review*, **124,** 1256–1271. https://doi.org/10.1175/1520-0493(1996)124<1256:DAUIAU>2.0.CO;2

Bühler, O., McIntyre, M. E., & Scinocca, J. F. (1999). On shear-generated gravity waves that reach the mesosphere. Part I: Wave generation. *Journal of Atmospheric Science*, **56**, 3749–3763. https://doi.org/10.1175/1520-0469(1999)056<3749:OSGGWT>2.0.CO;2

Chen, C., Chu, X., McDonald, A. J., Vadas, S. L., Yu, Z., Fong, W., & Lu, X. (2013). Inertiagravity waves in Antarctica: A case study using simultaneous lidar and radar measurements at McMurdo/Scott Base (77.8°S, 166.7°E). *Journal of Geophysical Research: Atmospheres*, **118**, 2794–2808. https://doi.org/10.1002/jgrd.50318

Chen, C., Chu, X., Zhao, J., Roberts, B. R., Yu, Z., Fong, W., et al. (2016). Lidar observations of persistent gravity waves with periods of 3–10 h in the Antarctic middle and upper atmosphere at McMurdo (77.83°S, 166.67°E). *Journal of Geophysical Research: Space Physics*, **121**, 1483–1502. https://doi.org/10.1002/2015ja022127

Chen, C., & Chu, X. (2017). Two-dimensional Morlet wavelet transform and its application to wave recognition methodology of automatically extracting two-dimensional wave packets from lidar observations in Antarctica. *Journal of Atmospheric and Solar-Terrestrial Physics*, **162**, 28–47. https://doi.org/10.1016/j.jastp.2016.10.016

Chu, X., Zhao, J., Lu, X., Harvey, V. L., Jones, R. M., Becker, E., et al. (2018). Lidar observations of stratospheric gravity waves from 2011 to 2015 at McMurdo (77.84°S, 166.69°E), Antarctica: 2. Potential energy densities, lognormal distributions, and seasonal variations. *Journal of Geophysical Research: Atmospheres*, **123**, 7910–7934. https://doi.org/10.1029/2017JD027386

Conn, A. R., Gould, N. I., & Toint, P. L. (2000). *Trust region methods*, Philadelphia, PA: Society for Industrial and Applied Mathematics. https://doi.org/10.1137/1.9780898719857

Dunkerton, T. J. (1981). On the inertial stability of the equatorial middle atmosphere. *Journal of the Atmospheric Sciences*, **38**, 2354–2364. https://doi.org/10.1175/1520-0469(1981)038%3C2354:OTISFT%3E2.0.CO;2

Dewan, E. M., & Good, R. E. (1986). Saturation and the "universal" spectrum for vertical profiles of horizontal scalar winds in the atmosphere. *Journal of Geophysical Research*, **91**(D2), 2742–2748. https://doi.org/10.1029/JD091iD02p02742

Dewan, E. M., Grossbard, N., Quesada, A. F. & Good, R. E. (1984). Spectral analysis of 10m resolution scalar velocity profiles in the stratosphere. *Geophysical Research Letters*, **11**, 80–83. https://doi.org/10.1029/GL011i001p00080

Ern, M., Ploeger, F., Preusse, P., Gille, J. C., Gray, L. J., Kalisch, S., Mlynczak, M. G,. Russell III, J. M., & Riese, M. (2014). Interaction of gravity waves with the QBO: A satellite perspective. *Journal of Geophysical Research: Atmospheres*, **119**, 2329–2355. https://doi.org/10.1002/2013JD020731

Ern, M., Trinh, Q. T., Preusse, P., Gille, J. C., Mlynczak, M. G., Russell Iii, J. M., & Riese, M. (2018). GRACILE: a comprehensive climatology of atmospheric gravity wave parameters based on satellite limb soundings. *Earth System Science Data*, **10**, 857–892. https://doi.org/10.5194/essd-10-857-2018

Fritts, D. C., & Alexander, M. J. (2003). Gravity wave dynamics and effects in the middle atmosphere. *Reviews of Geophysics*, **41**, 1003. https://doi.org/10.1029/2001RG000106

Fritts, D. C., & Chou, H. (1987). An Investigation of the Vertical Wavenumber and Frequency Spectra of Gravity Wave Motions in the Lower Stratosphere. *Journal of the Atmospheric Sciences*, **44**(24), 3610–3624. https://doi.org/10.1175/1520-0469(1987)044%3C3610:AIOTVW%3E2.0.CO;2

Hines, C. O. (1997a). Doppler-spread parameterization of gravity-wave momentum deposition in the middle atmosphere. Part 1: Basic formulation. *Journal of Atmospheric and Solar-Terrestrial Physics*, **59**, 371–386. https://doi.org/10.1016/S1364-6826(96)00079-X

Hines, C. O. (1997b). Doppler-spread parameterization of gravity-wave momentum deposition in the middle atmosphere. Part 2: Broad and quasi monochromatic spectra, and implementation. *Journal of Atmospheric and Solar-Terrestrial Physics*, **59**(4), 387–400. https://doi.org/10.1016/S1364-6826(96)00080-6

Holton, J. R. (1983). The influence of gravity wave breaking on the general circulation of the middle atmosphere. *Journal of the Atmospheric Sciences*, **40**, 2497–2507. https://doi.org/10.1175/1520-0469(1983)040%3C2497:TIOGWB%3E2.0.CO;2

Kawatani, Y., Sato, K., Dunkerton, T. J., Watanabe, S., Miyahara, S., & Takahashi, M. (2010a). The roles of equatorial trapped waves and internal inertia-gravity waves in driving the quasi-biennial oscillation. Part I: Zonal mean wave forcing. *Journal of the Atmospheric Sciences*, **67**, 963–980. https://doi.org/10.1175/2009JAS3222.1

Kawatani, Y., Sato, K., Dunkerton, T. J., Watanabe, S., Miyahara, S., & Takahashi, M. (2010b). The roles of equatorial trapped waves and internal inertia-gravity waves in driving the quasi-biennial oscillation. Part II: Three-dimensional distribution of wave forcing. *Journal of the Atmospheric Sciences*, **67**, 981–997. https://doi.org/10.1175/2009JAS3223.1

Koshin, D., Sato, K., Miyazaki, K., & Watanabe, S. (2020). An ensemble Kalman filter data assimilation system for the whole neutral atmosphere. *Geoscientific Model Development*, **13**, 3145–3177. https://doi.org/10.5194/gmd-13-3145-2020

Koshin, D., Sato, K., Kohma, M., & Watanabe, S. (2022). An update on the 4D-LETKF data assimilation system for the whole neutral atmosphere. *Geoscientific Model Development*. **5**, 2293–2307. https://doi.org/10.5194/gmd-15-2293-2022

Lu, X., Chu, X., Fong, W., Chen, C., Yu, Z., Roberts, B. R., & McDonald, A. J. (2015). Vertical evolution of potential energy density and vertical wave number spectrum of Antarctic gravity waves from 35 to 105 km at McMurdo (77.8°S, 166.7°E). *Journal of Geophysical Research: Atmospheres*, **120**, 2719–2737. https://doi.org/10.1002/2014JD022751

Mayr, H. G., Mengel, J. G., Hines, C. O., Chan, K. L., Arnold, N. F., Reddy, C. A., & Porter, H. S. (1997). The gravity wave Doppler spread theory applied in a numerical spectral model of the middle atmosphere 2. Equatorial oscillations. *Journal of Geophysical Research*, **102**, 26,093–26,105. https://doi.org/10.1029/96JD03214

McLandress, C., & Scinocca, J. F. (2005). The GCM Response to Current Parameterizations of Nonorographic Gravity Wave Drag. *Journal of the Atmospheric Sciences*, **62**(7), 2394–2413. https://doi.org/10.1175/JAS3483.1

Noersomadi & Tsuda, T. (2016). Global distribution of vertical wavenumber spectra in the lower stratosphere observed using high-vertical-resolution temperature profiles from COSMIC GPS radio occultation. *Annals of Geophysics*, **34**, 203–213. https://doi.org/10.5194/angeo-34-203-2016.

Okamoto, K., Sato, K., & Akiyoshi, H. (2011). A study on the formation and trend of the Brewer-Dobson circulation. *Journal of Geophysical Research*, **116**, D10117. https://doi.org/10.1029/2010JD014953

Okui, H., & Sato, K. (2020). Characteristics and Sources of Gravity Waves in the Summer Stratosphere Based on Long-Term and High-Resolution Radiosonde Observations. *SOLA*, **16**, 64–69. https://doi.org/10.2151/sola.2020-011

Okui, H., Sato, K., Koshin, D., & Watanabe, S. (2021). Formation of a mesospheric inversion layer and the subsequent elevated stratopause associated with the major stratospheric sudden warming in 2018/19. *Journal of Geophysical Research: Atmospheres*, **126**, e2021JD034681. https://doi.org/10.1029/2021JD034681

Rapp, M., Dörnbrack, A., & Preusse, P. (2018). Large midlatitude stratospheric temperature variability caused by inertial instability: A potential source of bias for gravity wave climatologies. *Geophysical Research Letters*, **45**, 10,682–10,690. https://doi.org/10.1029/2018GL079142

Sato, K. (1994). A statistical study of the structure, saturation and sources of inertio-gravity 905 waves in the lower stratosphere observed with the MU radar. *Journal of Atmospheric and Terrestrial Physics*, **56**(6), 755–774. https://doi.org/10.1016/0021-9169(94)90131-7

Sato, K., & Dunkerton, T. J. (1997). Estimates of momentum flux associated with equatorial Kelvin and gravity waves. *Journal of Geophysical Research*, **102**, 26,247–26,261. https://doi.org/10.1029/96JD02514

Sato, K. & Hirano, S. (2019). The climatology of the Brewer–Dobson circulation and the contribution of gravity waves. *Atmospheric Chemistry and Physics*, **19**, 4517–4539. https://doi.org/10.5194/acp-19-4517-2019

Sato, K., Tateno, S., Watanabe, S., & Kawatani, Y. (2012). Gravity Wave Characteristics in the Southern Hemisphere Revealed by a High-Resolution Middle-Atmosphere General Circulation Model. *Journal of the Atmospheric Sciences*, **69**, 1378–1396. https://doi.org/10.1175/JAS-D-11-0101.1

Sato, K., Watanabe, S., Kawatani, Y., Tomikawa, Y., Miyazaki, K., & Takahashi, M. (2009). On the origins of mesospheric gravity waves. *Geophysical Research Letters*, **36**, L19801. https://doi.org/10.1029/2009GL039908

Sato, K., & Yamada, M. (1994). Vertical structure of atmospheric gravity waves revealed by the wavelet analysis. *Journal of Geophysical Research*, **99**(D10), 20,623–20,631. https://doi.org/10.1029/94JD01818

Sato, K., Yamamori, M., Ogino, S., Takahashi, N., Tomikawa, Y., & Yamanouchi, T. (2003). A meridional scan of the stratospheric gravity wave field over the ocean in 2001 (MeSSO2001). *Journal of Geophysical Research*, **108**(D16), 4491. https://doi.org/10.1029/2002JD003219

Senft, D. C., & Gardner, C. S. (1991). Seasonal variability of gravity wave activity and spectra in the mesopause region at Urbana. *Journal of Geophysical Research*, **96**, 17,229–17,264. https://doi.org/10.1029/91JD01662

Smith, S. A., Fritts, D. C., & Vanzandt, T. E. (1987). Evidence for a Saturated Spectrum of Atmospheric Gravity Waves. *Journal of the Atmospheric Sciences*, **44**(10), 1404–1410. https://doi.org/10.1175/1520-0469(1987)044%3C1404:EFASSO%3E2.0.CO;2

Stephan, C. C., Strube, C., Klocke, D., Ern, M., Hoffmann, L., Preusse, P., & Schmidt, H. (2019). Intercomparison of gravity waves in global convection-permitting models. *Journal of the Atmospheric Sciences*, **76**, 2739–2759. https://doi.org/10.1175/JAS-D-19-0040.1

Strube, C., Ern, M., Preusse, P., & Riese, M. (2020). Removing spurious inertial instability signals from gravity wave temperature perturbations using spectral filtering methods. *Atmospheric Measurement Techniques*, **13**, 4927–4945. https://doi.org/10.5194/amt-13-4927-2020

Tsuda, T., Inoue, T., Kato, S., Fukao, S., Fritts, D. C., & VanZandt, T. E. (1989). MST Radar Observations of a Saturated Gravity Wave Spectrum. *Journal of the Atmospheric Sciences*, **46**(15), 2440–2447. https://doi.org/10.1175/1520-0469(1989)046%3C2440:MROOAS%3E2.0.CO;2

Tsuda, T., Kato, S., Yokoi, T., Inoue, T., Yamamoto, M., Vanzandt, T. E., Fukao, S., & Sato, T. (1990). Gravity waves in the mesosphere observed with the middle and upper atmosphere radar. *Radio Science*, **25**(5), 1005–1018. https://doi.org/10.1029/RS025i005p01005

Tsuda, T., Lin, X., Hayashi, H., & Noersomadi (2011). Analysis of vertical wave number spectrum of atmospheric gravity waves in the stratosphere using COSMIC GPS radio occultation data. *Atmospheric Measurement Techniques*, **4**, 1627–1636. https://doi.org/10.5194/amt-4-1627-2011

VanZandt, T. E. (1982). A universal spectrum of buoyancy waves in the atmosphere. *Geophysical Research Letters*, **9**, 575–578. https://doi.org/10.1029/GL009i005p00575

VanZandt, T. E. (1985). A model for gravity wave spectra observed by Doppler sounding systems. *Radio Science*, **20**(6), 1323–1330. https://doi.org/10.1029/RS020i006p01323

Wang, L., Geller, M. A., & Alexander, M. J. (2005). Spatial and Temporal Variations of Gravity Wave Parameters. Part I: Intrinsic Frequency, Wavelength, and Vertical Propagation Direction. *Journal of the Atmospheric Sciences*, **62**(1), 125–142. https://doi.org/10.1175/JAS-3364.1

Warner, C. D., & McIntyre, M. E. (1996). On the Propagation and Dissipation of Gravity Wave Spectra through a Realistic Middle Atmosphere. *Journal of the Atmospheric Sciences*, **53**(22), 3213–3235. https://doi.org/10.1175/1520-0469(1996)053%3C3213:OTPADO%3E2.0.CO;2

Warner, C. D. & McIntyre, M. E. (1999). Toward an ultra-simple spectral gravity wave parameterization for general circulation models. *Earth, Planets and Space*, **51**, 475–484. https://doi.org/10.1186/BF03353209

Watanabe, S. (2008). Constraints on a Non-orographic Gravity Wave Drag Parameterization Using a Gravity Wave Resolving General Circulation Model. *SOLA*, **4**, 61–64. https://doi.org/10.2151/sola.2008-016

Watanabe, S., & Miyahara, S. (2009). Quantification of the gravity wave forcing of the migrating diurnal tide in a gravity wave-resolving general circulation model. *Journal of Geophysical Research: Atmospheres*, **114**, D07110. https://doi.org/10.1029/2008JD011218

Watanabe, S., Sato, K., Kawatani, Y., & Takahashi, M. (2015). Vertical resolution dependence of gravity wave momentum flux simulated by an atmospheric general circulation model. *Geoscientific Model Development*, **8**, 1637–1644. https://doi.org/10.5194/gmd-8-1637-2015

Yan, Y. Y., Zhang, S. D., Huang, C. M., Huang, K. M., Gong, Y., & Gan, Q. (2018). The vertical wave number spectra of potential energy density in the stratosphere deduced from the COSMIC satellite observation. *Quarterly Journal of the Royal Meteorological Society*, **145**, 318–336. https://doi.org/10.1002/qj.3433

Zhao, J., Chu, X., Chen, C., Lu, X., Fong, W., Yu, Z., Jones, R. M., Roberts, B. R., & Dörnbrack, A. (2017). Lidar observations of stratospheric gravity waves from 2011 to 2015 at McMurdo (77.84°S, 166.69°E), Antarctica: 1. Vertical wavelengths, periods, and frequency and vertical wave number spectra. *Journal of Geophysical Research: Atmospheres*, **122**(10), 5041–5062. https://doi.org/10.1002/2016jd026368